A Systematic Account on Aromatic Hydroxylation by a Cytochrome P450 Model Compound I

DOI:
10.1002/chem.201604361

Document Version
Accepted author manuscript

Published in:
Chemistry - A European Journal

A systematic account on aromatic hydroxylation by a cytochrome P450 model Compound I: A low-pressure mass spectrometry and computational study

Fabián G. Cantú Reinhard,[a]† Mala A. Sainna,[a]† Pranav Upadhayay,[b] G. Alex Balan,[a] Devesh Kumar,[b] Simonetta Fornarini,*[c] Maria Elisa Crestoni,*[c] and Sam P. de Visser*[a]

Abstract: Cytochrome P450 enzymes are heme containing mono-oxygenases that mainly react through oxygen atom transfer. Specific features of substrate and oxidant that determine the reaction rate constant for oxygen atom transfer are still poorly understood and, therefore, we did a systematic gas-phase study on reactions by iron(IV)-oxo porphyrin cation radical structures with arenes. We present here the first results obtained by using Fourier transform-ion cyclotron resonance mass spectrometry and provide rate constants and product distributions for the assayed reactions. Product distributions and kinetic isotope effect studies implicate a rate determining aromatic hydroxylation reaction that correlates with the ionization energy of the substrate and no evidence of aliphatic hydroxylation products is observed. To further understand the details of the reaction mechanism, a computational study on a model complex was performed. These studies confirm the experimental hypothesis of dominant aromatic over aliphatic hydroxylation and show that the lack of an axial ligand affects the aliphatic pathways. Moreover, a two parabola valence bond model is used to rationalize the rate constant and identify key properties of the oxidant and substrate that drive the reaction. In particular, the work shows that aromatic hydroxylation rates correlate with the ionization energy of the substrate as well as with the electron affinity of the oxidant.

Introduction

Aromatic hydroxylation is a challenging catalytic reaction because a very strong C–H bond of a substrate needs to be broken in the process. Several enzymes in nature have developed procedures to enable an aromatic hydroxylation or even a dioxygenation;[1] Among those are the nonheme iron dioxygenases that regio- and stereospecifically dihydroxylate an aromatic substrate into a catechol.[2] Highly relevant for environmental purposes are, for instance, the naphthalene dioxygenases that have functions in biotechnology that include the cleaning up of oil-spills and removal of aromatic compounds from soil.[3] Also, in the human body applications of heme and nonheme iron dioxygenases are found, for instance, for the biodegradation of aromatic amino acids starting with a mono- or dihydroxylation reaction.[4] Further arene activating enzymes in the body include the thiolate-ligated heme mono-oxygenases called cytochromes P450 (P450) that have been shown to hydroxylate arenes to phenols as a means to metabolize drugs as well as xenobiotic molecules in the liver.[5]

The full details of the mechanism of the latter processes are still shrouded in many mysteries and so far no experimental reaction rates have been obtained. Progress in understanding the P450-type reaction mechanisms has been made in the fields of computational chemistry and low-pressure mass spectrometry.[6,7] In particular, some of us have utilized Fourier transform-ion cyclotron resonance mass spectrometry (FT-ICR MS) to trap and characterize a pentacoordinated model complex of the active species of P450 enzymes (Compound I, CpdI).[8] We have utilized this experience and measured low-pressure thermal rate constants of aromatic hydroxylation by this CpdI model for the first time and present these results here.

P450 CpdI is a high-valent iron(IV)-oxo heme cation radical, which is bound to the enzyme through a thiolate bridge of a conserved cysteinate residue. It has been spectroscopically trapped and characterized at low temperature for one specific isozyme, but for only very few substrates experimental rate constants could be determined due to its short lifetime.[9] As such much has to be gained from understanding the reactivity patterns of CpdI with substrates and particularly on the regioselectivity and bifurcation patterns leading to a variety of products. On the other hand, CpdI and its reactivity patterns with substrates have been extensively studied with computational methods and detailed mechanisms of aromatic and aliphatic hydroxylation as well as sulfoxidation were established.[10]

Figure 1 shows the active site description of P450 CYP120A1 with the heme and its link to Cys_{391} highlighted. These crystal structure coordinates contain retinoic acid as substrate in the vicinity of the heme on its distal site.[11] CpdI was shown to be a versatile oxidant and to react efficiently with a variety of different substrates. In our previous work we reported a combined mass spectrometric and computational study on a biomimetic model of CpdI, where the protoporphyrin IX was replaced by 5,10,15,20-tetrakis(pentafluorophenyl) porphyrin (TPFPP), Figure 1b.[12] The ensuing $[Fe^{IV}(O)(TPFPP^{+\bullet})]^{+}$ cation was trapped in the cell of an FT-ICR mass spectrometer and its reactivity studied with a selection of olefins.

[a] F.G. Cantú Reinhard, Dr M.A. Sainna, G.A. Balan, Dr S.P. de Visser
Manchester Institute of Biotechnology and School of Chemical Engineering and Analytical Science
The University of Manchester, 131 Princess Street, Manchester M1 7DN, United Kingdom
sam.devisser@manchester.ac.uk

[b] P. Upadhayay, Dr D. Kumar
Department of Applied Physics, School for Physical Sciences, Babasaheb Bhimrao Ambedkar University, Vidya Vihar, Rae Bareilly Road, Lucknow (UP) 226025, India
dkclcre@yahoo.com

[c] Prof. Dr. S. Fornarini, Prof. Dr. M.E. Crestoni
Dipartimento di Chimica e Tecnologie del Farmaco,
Università di Roma "La Sapienza", P.le A. Moro 5, 00185, Roma, Italy
mariaelisa.crestoni@uniroma1.it; simonetta.fornarini@uniroma1.it

† These authors contributed equally.

Supporting information for this article is given via a link at the end of the document.

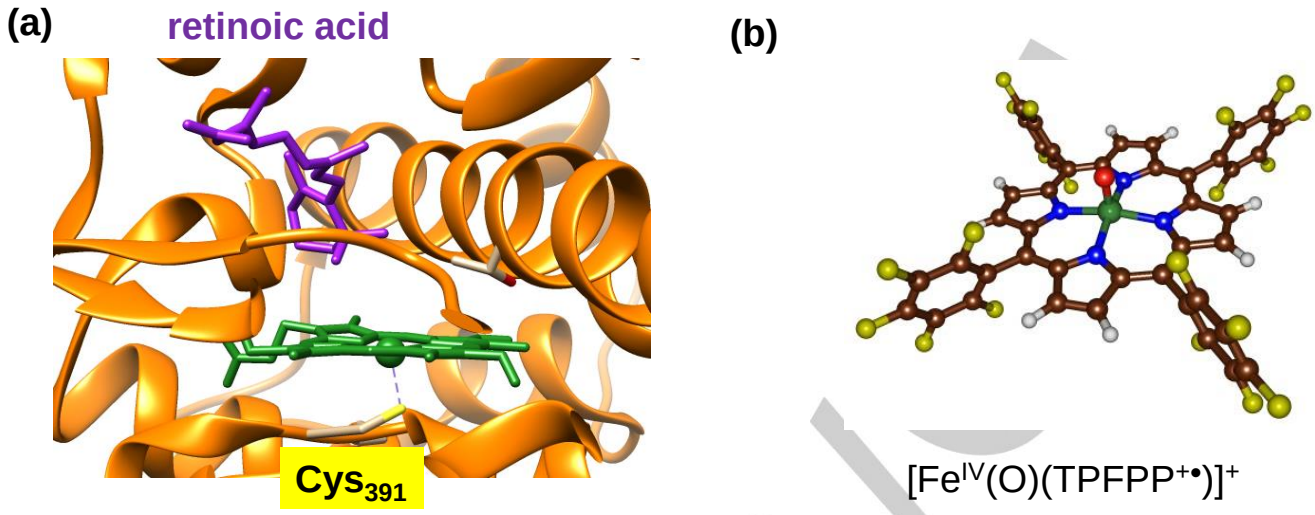

Figure 1. Enzymatic and biomimetic models of cytochrome P450 CpdI. (a) active site structure as taken of substrate bound-resting state P450 from the 2VE3 pdb file. (b) biomimetic model investigated here.

These studies established rate constants for olefin epoxidation showing them to correlate with the ionization energy (IE) of the substrate that is activated. Subsequently, density functional theory (DFT) calculations confirmed the observed trend and using a valence bond (VB) scheme highlighted the major components of the oxidant and substrate that contribute to the free energy of activation. To gain further insight into the reactivity patterns of CpdI model complexes using a combined FT-ICR MS and DFT approach, we decided to follow up our studies with work on aromatic hydroxylation. We propose a nucleophilic addition pathway as rate determining reaction step, whereby the rate is determined by the ionization potential of the substrate and the π/π^* energy splitting of the CpdI models as well as electron reorganization energies within the complex. Furthermore, it is found that the removal of the axial cysteinate ligand as in the FT-ICR MS model used here raises the energies of the aliphatic hydroxylation pathways dramatically and prevents these product channels. The studies, therefore, give evidence of the axial ligand to be crucial in determining the activity and potential of the reactive oxidant of P450 enzymes.

Results

Experiment. In previous work, we established working procedures for the trapping of high-valent transition metal-oxo intermediates in an FT-ICR MS.[7,12] These studies identified structures with m/z 1044 in the mass spectrum representing $[Fe^{IV}(O)(TPFPP^{+\bullet})]^+$ ions in good abundance and with long enough lifetime to enable ion-molecule reactions in the gas-phase. These procedures enabled us to do a systematic study into olefin epoxidation by these ions,[12] which established reactivity trends and a model that accounts for the observed reactivity. We decided to follow the study up with a systematic account on arene hydroxylation processes. In particular, a series of 16 aromatic substrates were investigated and their second-order rate constants (k_{exp}) in a reaction with $[Fe^{IV}(O)(TPFPP^{+\bullet})]^+$ determined. Note that due to bifurcation processes multiple reaction channels and products are possible leading to aromatic and aliphatic hydroxylation products. Using ADO theory (see Methods), the experimental rate constants were converted into reaction efficiencies (Φ) that represent the fraction of reactive collisions.

Table 1 summarizes the experimentally determined reaction rates for all substrates as well as their individual product distributions. Also included are ionization energies (IE) taken from the NIST database.[13] Thus, the reaction of $[Fe^{IV}(O)(TPFPP^{+\bullet})]^+$ with arenes typically gives two reaction channels, namely oxygen atom transfer (OAT) and an addition process (Add), see Scheme 1. The OAT reaction leads to the formation of $[Fe^{III}(TPFPP)]^+$ ions with m/z 1028, and, consequently release of oxygenated substrate. In addition, in several cases an adduct complex is observed with mass corresponding to $[Fe^{III}(TPFPP)(SubO)]^+$, whereby Sub represents the substrate.

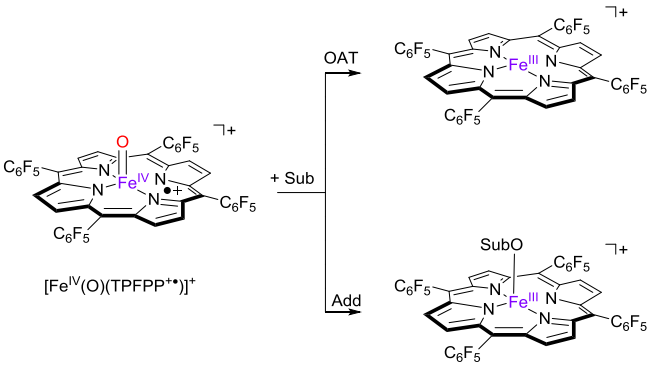

Scheme 1. Reaction products observed from the reaction of $[Fe^{IV}(O)(TPFPP^{+\bullet})]^+$ with arenes (Sub).

Table 1. FT-ICR MS reactivity of $[Fe^{IV}(O)(TPFPP^{+\bullet})]^+$ with arenes: Second-order rate constants, reaction efficiencies and product distributions (OAT and Add)

Substrate	IE [a]	k_{exp} [b, c]	k_{ADO} [b]	Φ_{OAT}	Φ_{Add}	%OAT	%Add
benzaldehyde	9.50	0.15	11.4	–	1.3	0	100
α-[D_1]-benzaldehyde	9.50	0.14	11.4	–	1.2	0	100
benzene	9.20	0.012	8.8	0.14	–	100	–
toluene	8.80	0.36	9.2	3.1	0.78	80	20
ethylbenzene	8.77	0.58	9.5	4.3	1.8	70	30
[D_5]-ethylbenzene	8.77	0.56	9.5	4.2	1.7	72	28
[D_{10}]-ethylbenzene	8.77	0.57	9.5	4.4	1.6	73	27
i-propylbenzene	8.73	1.2	10.0	7.8	4.2	65	35
t-butylbenzene	8.68	1.0	10.0	9.5	0.5	95	5
o-xylene	8.56	1.4	9.5	9.5	5.2	65	35
[D_4]-o-xylene	8.56	1.4	9.5	9.1	5.6	62	38
[D_6]-o-xylene	8.56	1.3	9.5	8.9	4.8	65	35
m-xylene	8.55	1.6	9.5	15.8	1.2	93	7
p-xylene	8.44	1.3	8.9	9.4	5.1	65	35
mesitylene	8.40	1.9	9.0	12.6	8.4	60	40
naphthalene	8.14	0.93	9.1	7.6	2.4	76	24

[a] from NIST database, in eV. [b] second-order rate constants (k_{exp}) in units of 10^{-10} cm^3 $molecule^{-1}$ s^{-1}, at the temperature of the FT-ICR cell (300K). [c] The estimated error is ±30%; the internal consistency of the data is within ±10%.

Figure S1 in the Supplementary Information shows an example of a mass spectrum recorded along the kinetic run for the reaction of $[Fe^{IV}(O)(TPFPP^{+\bullet})]^+$ with toluene at 3.8×10^{-8} mbar and displays signals at 120 s reaction time for the reactant $[Fe^{IV}(O)(TPFPP^{+\bullet})]^+$ centered at m/z 1044, product ions $[Fe^{III}(TPFPP)]^+$ at m/z 1028, and $[Fe^{III}(TPFPP)(SubO)]^+$ at m/z 1136.

The actual formation of an oxidation product remaining in the coordination sphere of $[Fe^{III}(TPFPP)]^+$ assigned to the $[Fe^{III}(TPFPP)(SubO)]^+$ ion at m/z 1136 has been verified by isolating the complex and submitting it to low-energy collision induced dissociation. As shown in Figure S2, the ion at m/z 1136 undergoes fragmentation releasing $[Fe^{III}(TPFPP)]^+$ by loss of SubO, namely the oxidation product of toluene. Additional evidence for the formation of a SubO ligand is inferred from a reaction that is observed at longer reaction times whereby the $[Fe^{III}(TPFPP)(SubO)]^+$ ion undergoes a ligand substitution process by a Sub molecule, the neutral present in the FT-ICR cell, to give $[Fe^{III}(TPFPP)(Sub)]^+$. This process is clearly observed for the reaction of benzaldehyde. In this case, one finds that the efficiency for the $[Fe^{III}(TPFPP)(SubO)]^+ + Sub \rightarrow [Fe^{III}(TPFPP)(Sub)]^+ + SubO$ reaction is less than 1.3% (this value represents the efficiency for the $[Fe^{IV}(O)(TPFPP^{+\bullet})]^+ + Sub \rightarrow [Fe^{III}(TPFPP)(SubO)]^+$ reaction, with Sub equal to benzaldehyde).

On this basis, an indirect probe for the structure of $[Fe^{III}(TPFPP)(SubO)]^+$ ions has been sought by forming distinct model complexes and studying their gas phase reactivity towards benzaldehyde. In methanol solution $[Fe^{III}(TPFPP)]^+$ reacts with both (m/p)-hydroxy-benzaldehyde and benzoic acid to give an addition complex which is delivered by electrospray ionization (ESI) into the gas phase, led into the ICR cell and tested for bimolecular reactivity with benzaldehyde. The complex with benzoic acid is found to be substantially more reactive in the ligand transfer process than both complexes with (m/p)-hydroxy-benzaldehyde (reaction efficiencies are equal to 14% and ca. 0.60%, respectively, Eq 1 – 3). This result is indicative that the gas phase oxidation of benzaldehyde by $[Fe^{IV}(O)(TPFPP^{+\bullet})]^+$ is directed at the aromatic ring rather than at the formyl group. The same experiment could not be extended to other substrates, given the scant ligand transfer reactivity typically displayed by arenes, but this outcome in the favorable case of benzaldehyde suggests that $[Fe^{IV}(O)(TPFPP^{+\bullet})]^+$ prefers attack at the aromatic ring rather than at a side chain substituent.

$[Fe^{III}(TPFPP)(C_6H_5COOH)]^+ + C_6H_5CHO \rightarrow [Fe^{III}(TPFPP)(C_6H_5CHO)]^+ + C_6H_5COOH,$
$\Phi = 14\%$ (1)

$[Fe^{III}(TPFPP)(p\text{-}OH\text{-}C_6H_4CHO)]^+ + C_6H_5CHO \rightarrow [Fe^{III}(TPFPP)(C_6H_5CHO)]^+ + p\text{-}OH\text{-}C_6H_4CHO,$
$\Phi = 0.64\%$ (2)

$[Fe^{III}(TPFPP)(m\text{-}OH\text{-}C_6H_4CHO)]^+ + C_6H_5CHO \rightarrow [Fe^{III}(TPFPP)(C_6H_5CHO)]^+ + m\text{-}OH\text{-}C_6H_4CHO,$
$\Phi = 0.56\%$ (3)

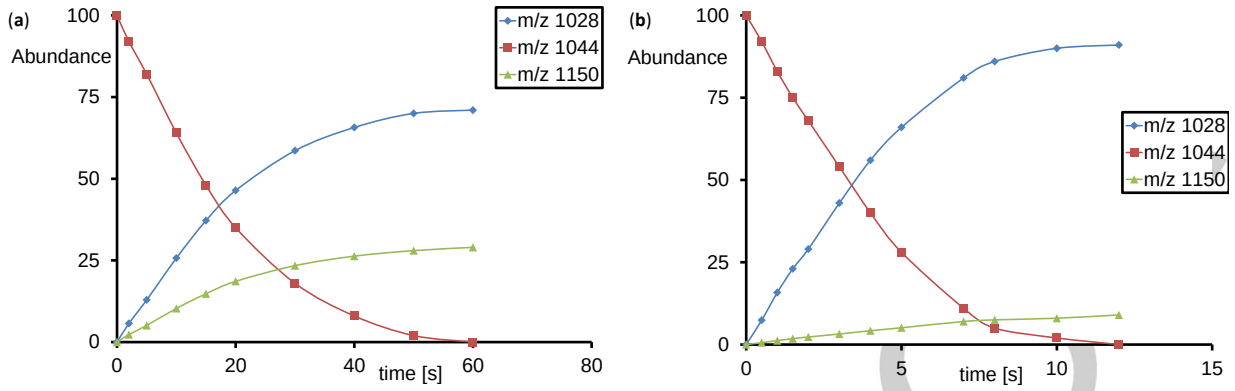

Figure 2. Ion distributions as a function of time for the reaction of $[Fe^{IV}(O)(TPFPP^{+\bullet})]^+$ with (a) ethylbenzene and (b) m-xylene.

As follows from Table 1 the rate constant ranges from 0.012 × 10^{-10} cm^3 s^{-1} for the reaction of $[Fe^{IV}(O)(TPFPP^{+\bullet})]^+$ with benzene increasing to a value of 1.9 × 10^{-10} cm^3 s^{-1} for the one with mesitylene. As such a spread of two orders of magnitude in rate constant is found for the series of substrates investigated here. In all cases (except for benzaldehyde) the dominant product complex obtained is the $[Fe^{III}(TPFPP)]^+$ ion representing the OAT channel. However, addition products are obtained in significant amounts with percentages of up to 40% (with mesitylene), whereas for benzaldehyde this is the sole reaction channel. Figure 2 displays the reactant and product abundancies as a function of time for the reaction of $[Fe^{IV}(O)(TPFPP^{+\bullet})]^+$ with ethylbenzene and m-xylene. The reactant ion abundance decays according to pseudo first-order kinetics as expected for a bimolecular reaction in the gas-phase. Thus, the ion abundance at m/z 1044 decays slowly as a function of time as the $[Fe^{IV}(O)(TPFPP^{+\bullet})]^+$ reacts away and the decay patterns were used to establish the experimental second-order rate constants k_{exp}. In the case of ethylbenzene as a substrate (Figure 2a) two products are formed with m/z 1028 and m/z 1150 representing the OAT and Add channels. The shape of the curves shown in Figure 2 is used to determine the efficiencies Φ_{OAT} and Φ_{Add} described in Table 1. As follows the ratio of the abundancies of the OAT and Add channels are constant as a function of time for ethylbenzene as well as m-xylene with ratios of m/z 1028:m/z 1150 of 2.5 and 13, respectively. This implies that these products originate from the same source and most probably, product release from the iron(III) complex is a slow process.

To find out whether the reactivities and, in particular, the product distributions relate to aromatic or aliphatic hydroxylation pathways, we repeated some of the reactions with deuterated substrates. Thus, we tested ethylbenzene with all aliphatic hydrogen atoms replaced by deuterium ($[D_5]$-ethylbenzene) and fully deuterated ethylbenzene ($[D_{10}]$-ethylbenzene). As can be seen from Table 1, the substrate deuteration has a small but non-significant effect on the reaction efficiencies and product distributions. Therefore, it can be concluded that the reaction between $[Fe(O)(TPFPP^{+\bullet})]^+$ and ethylbenzene does not proceed with a rate-determining hydrogen atom abstraction. The indication is rather that these reactions with deuterated substrates strongly implicate an aromatic hydroxylation of substrates. The product ratios also suggest that an ethylphenol product (as obtained from ethylbenzene) is more strongly bound to the iron(III) complex than the dimethylphenol product obtained from m-xylene.

To further confirm the reactions as aromatic hydroxylation, we investigated o-xylene with all aromatic hydrogen atoms replaced by deuterium ($[D_4]$-o-xylene) and all aliphatic hydrogen atoms replaced by deuterium ($[D_6]$-o-xylene). Table 1 gives the product distributions and reaction efficiencies for o-xylene, $[D_4]$-o-xylene and $[D_6]$-o-xylene. Within our experimental error margin all reaction efficiencies, rate constants and product distributions are the same, which gives evidence that in the reaction of $[Fe(O)(TPFPP^{+\bullet})]^+$ with o-xylene no rate determining hydrogen atom abstraction takes place.

Theory. To support the experiments and gain insight into the details of the reaction mechanism, we followed the work up with an extensive density functional theory (DFT) study to establish reactivity trends. Our initial work was aimed at the aromatic hydroxylation mechanism of arenes by $^{4,2}[Fe^{IV}(O)(TPFPP^{+\bullet})]^+$, although we utilized a model without porphyrin substituents here, i.e. porphyrin (Por). The investigated arenes in this work were mesitylene (**1**), toluene (**2**), ethylbenzene (**3**), fluorobenzene (**4**), chlorobenzene (**5**), naphthalene (**6**), i-propylbenzene (**7**) and t-butylbenzene (**8**). Test calculations with the full TPFPP model were also performed but found to give only minor differences in structure and reactivity with respect to the smaller porphyrin complex without side groups (see Supporting Information). Figure 3 shows the aromatic hydroxylation reaction of the para-position of toluene (PhMe; henceforth indicated with the subscript 2 beside the label of the structure) by the doublet and quartet spin states of $[Fe^{IV}(O)(Por^{+\bullet})]^+$ as calculated with DFT as an example. Thus, the reaction starts with an electrophilic attack of the oxo group on the para-carbon atom of the substrate that via a transition state **TS1** leads to the intermediate **I1**. As shown previously by calculations on P450 model complexes, the ipso-proton is abstracted by the porphyrin group via transition state **TS2** to form the protonated porphyrin structure **I2**. Finally, the proton is relayed to the phenolate group via transition state **TS3** to form phenol products (**P**).[14]

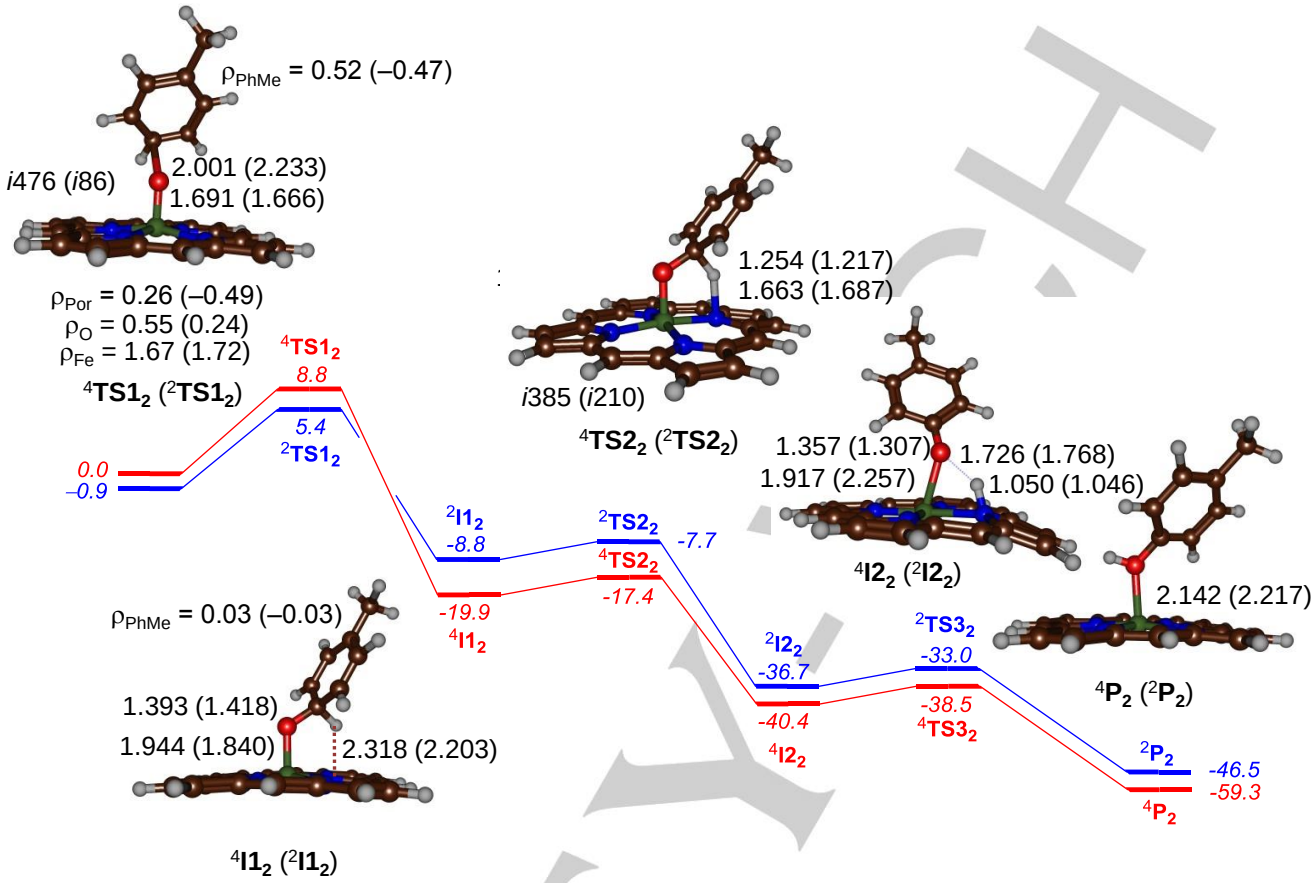

Figure 3. Potential energy profile (in kcal mol^{-1}) of aromatic hydroxylation of toluene (PhMe) by $[Fe^{IV}(O)(Por^{+\bullet})]^{+}$ as calculated with DFT at UB3LYP/BS2//UB3LYP/BS1 level of theory. All data include ZPE corrections and are calculated relative to isolated reactants. Bond lengths are given in angstroms and group spin densities (ρ) in atomic units.

An analysis of the group spin densities and charges establishes the intermediates **I1** as cationic on the substrate moiety (ρ_{PhMe} = 0.03/–0.03 in ^{4}**I1**$_2$/^{2}**I1**$_2$), which implies that two electrons have transferred from substrate to oxidant. We made several attempts to find radical intermediates through the swapping of molecular orbitals, but in all of these cases the wave functions converged back to the cationic intermediates instead. Recent experimental studies of Asaka and Fujii found experimental evidence of fast electron transfer during the C–O bond formation step and hence support the formation of a cationic intermediate.[15]

After the cationic intermediates (**I1**) the substrate loses its ipso-proton to the porphyrin ring via a small reaction barrier of 2.5 kcal mol^{-1} on the quartet spin state and 1.1 kcal mol^{-1} on the doublet spin surface. This proton-transfer intermediate (**I2**) then relays the proton back to the phenolate oxygen atom to form phenol products via another transition state **TS3** lying close in energy to **I2**.

The rate determining step in the reaction mechanism, however, is the electrophilic addition step via **TS1**, which elongates the Fe–O bond to 1.691/1.666 Å in ^{4,2}**TS1**$_2$ and has the substrate in an almost upright position. An analysis of the group spin densities (ρ) establishes it as a radical-type transition state with spin densities of 2.22 (1.96), 0.26 (–049) and 0.52 (–0.47) on the FeO, Por and PhMe groups, respectively, in ^{4}**TS1**$_2$ (^{2}**TS1**$_2$). As the reactant state has an electronic configuration $\pi^{*}_{xz}{}^{1}\ \pi^{*}_{yz}{}^{1}\ a_{1u}{}^{1}$ with spin density of about 2 on the FeO group and 1 on the porphyrin ring, this implies that radical character on the porphyrin manifold is lost in the transition state. In particular, an electron transfer from substrate into the a_{1u} orbital has occurred to create a transition state with configuration approximating $\pi^{*}_{xz}{}^{1}\ \pi^{*}_{yz}{}^{1}\ a_{1u}{}^{2}\ \phi_{PhMe}{}^{1}$.

After the transition state the system relaxes to the cationic intermediate **I1**, which involves a second electron transfer from the substrate to the metal to generate an intermediate with orbital occupation $\pi^{*}_{xz}{}^{1}\ \pi^{*}_{yz}{}^{1}\ \sigma^{*}_{z2}{}^{1}\ a_{1u}{}^{2}\ \phi_{PhMe}{}^{0}$. Geometrically, this second electron transfer and the single occupation of the σ^{*}_{z2} orbital results in considerable lengthening of the Fe–O bond from 1.691 Å in ^{4}**TS1**$_2$ to 1.944 Å in ^{4}**I1**$_2$. At the same time the C–O distance shortens from 2.001 Å in the transition state to 1.393 Å in the intermediate.

In the subsequent step we located transition states for proton transfer from the ipso-position to one of the nitrogen atoms of the porphyrin ligand in the doublet and quartet spin states. These proton transfer barriers have a relatively small imaginary frequency, i385 cm^{-1} (^{4}**TS2**$_2$) and i210 cm^{-1} (^{2}**TS2**$_2$), as compared to typical hydrogen atom abstraction transition states where values of well over i1000 cm^{-1} were found.[16]

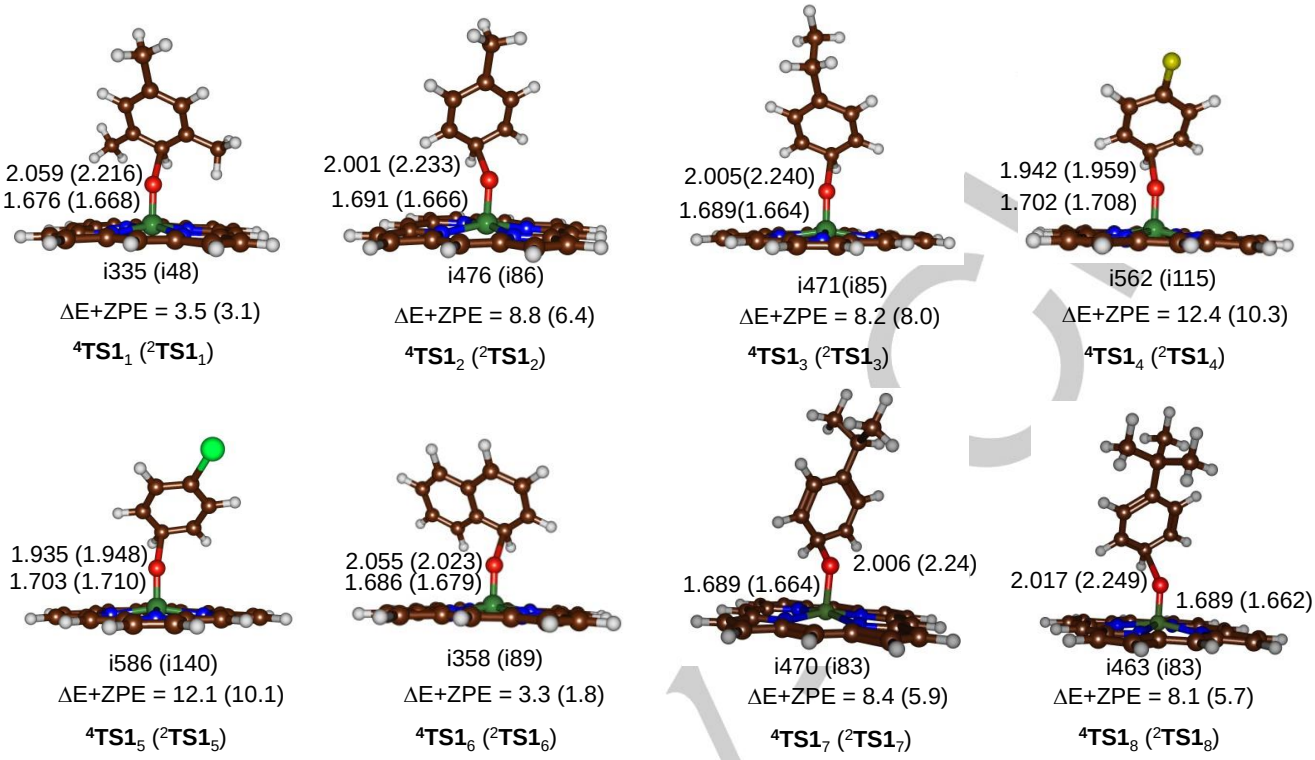

Figure 4. Optimized electrophilic addition transition states for the reaction of $^{4,2}[Fe^{IV}(O)(Por^{+\bullet})]^{+}$ with arenes. Barrier heights (in kcal mol^{-1}) given are relative to isolated reactants and calculated at UB3LYP/BS2//UB3LYP/BS1 level of theory. Bond lengths are in angstroms and imaginary frequencies in wave numbers.

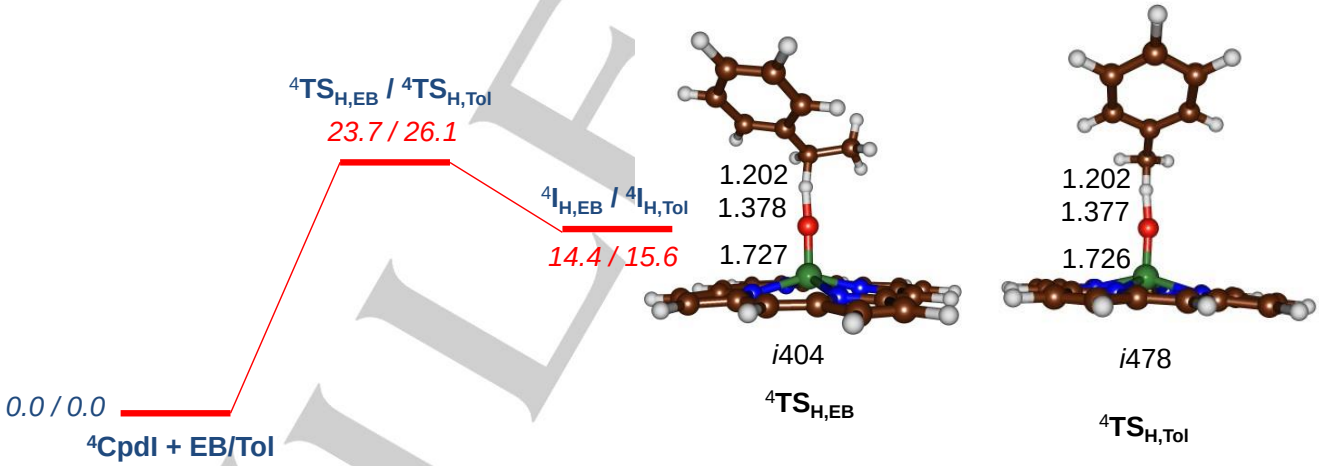

Figure 5. Aliphatic hydroxylation potential energy landscape as calculated at UB3LYP/BS2//UB3LYP/BS1 level of theory. Energies are in kcal mol^{-1} and include ZPE correction, while geometries give bond distances in angstroms and the imaginary frequency in wave numbers.

From the **I2** intermediates another proton transfer leads to the phenol product complexes with high exothermicity. A small barrier **TS3** is obtained in both spin states.

Overall, the aromatic hydroxylation reaction is stepwise with a rate determining electrophilic addition step with a barrier of $\Delta E^{\ddagger}$+ZPE = 8.8 (5.4) kcal mol^{-1} on the quartet (doublet) spin states. These values compare well with previous studies of aliphatic and aromatic hydroxylation by iron(IV)-oxo porphyrin cation radical complexes.[12,16–18]

Thereafter, we completed the investigation of $^{4,2}[Fe^{IV}(O)(Por^{+\bullet})]^{+}$ and its aromatic hydroxylation of a range of arenes and initially calculated the full landscape for chlorobenzene hydroxylation by $^{4,2}[Fe^{IV}(O)(Por^{+\bullet})]^{+}$, see Supporting Information for details. The landscape gives the same pattern as that seen for toluene in Figure 3 with a rate-determining electrophilic addition barrier **TS1$_5$** leading to a cationic intermediate **I1$_5$**. Similarly to the toluene data reported above, ^{2}**TS1$_5$** is below ^{4}**TS1$_5$** as seen before in aromatic hydroxylation by P450 CpdI models.[14]

In addition, we calculated ^{4,2}**TS1** and ^{4,2}**I1** for the following substrates: mesitylene, ethylbenzene, fluorobenzene, naphthalene, i-propylbenzene and t-butylbenzene, whereby we give the label as a subscript after the structure name. In general, the same structural trends are observed in the quartet and doublet spin states and the mechanism is the same.

As can be seen strong geometric differences are found upon changing the para-substituent of the arene, whereby the ^{4}**TS1** structures for fluorobenzene gives Fe–O and O–C distances of 1.703 and 1.942 Å, while with ethylbenzene these distances change to 1.689 and 2.005 Å, respectively. Similar differences are seen for the other complexes as well as in the value of the imaginary frequency in the transition state. Nevertheless, all **TS1** structures shown in Figure 4 represent the same electronic transition of electron transfer from arene to a_{1u} and the accumulation of radical character on the arene group. Moreover, the transition state structures are geometrically alike with the substrate in virtually the same orientation in all cases. The occurrence of an electron transfer equilibrium preceding aromatic hydroxylation by a compound I model within a solvent cage has been highlighted.[15] The electrophilic addition transition states shown in Figure 4 differ strongly in the barrier height and values of $\Delta E^{\ddagger}$+ZPE range from 1.8 kcal mol^{-1} for ^{2}**TS$_6$** (naphthalene) to 12.4 kcal mol^{-1} for ^{4}**TS1$_4$** (fluorobenzene). Nevertheless, all of them are radical type transition states with group spin densities similar to those reported for ^{4,2}**TS1**$_2$ reported above in Figure 3.

To ascertain that the lowest energy pathway indeed is aromatic hydroxylation rather than aliphatic hydroxylation, we also calculated the aliphatic hydroxylation mechanisms of toluene and ethylbenzene by ^{4}[Fe^{IV}(O)(Por$^{+\bullet}$)]$^{+}$, see Figure 5. These reactions are also stepwise with an initial hydrogen atom abstraction via transition state ^{4}**TS**$_H$ that leads to a radical intermediate ^{4}**I**$_H$. In both aliphatic hydrogen atom abstraction transition states significant radical character (ρ = –0.52 for both) is obtained. In a subsequent radical rebound barrier the OH group is transferred to substrate to form alcohol product complexes ^{4}**P**$_H$. The hydrogen atom abstraction is rate determining and has a relatively central transition state with elongated C–H distances of 1.202 Å for both toluene and ethylbenzene. In both structures the Fe–O bond has elongated to well over 1.7 Å.

Energetically, the hydrogen atom abstraction barriers are higher than the arene activation barriers **TS1** shown in Figure 4 by well over 15 kcal mol^{-1}. Therefore, the dominant pathway is expected to be aromatic hydroxylation of arenes by [Fe^{IV}(O)(Por$^{+\bullet}$)]$^{+}$ and little or no aliphatic hydroxylation products should be observed. The [Fe^{IV}(O)(Por$^{+\bullet}$)]$^{+}$ system, as a consequence, reacts sluggishly with aliphatic groups, in contrast to iron(IV)-oxo porphyrins with an anionic axial ligand. Previously, we and others showed that the barrier heights of aliphatic hydroxylation reactions correlate with the bond dissociation energy (BDE_{OH}) for the formation of the iron(IV)-hydroxo species from the iron(IV)-oxo species and a hydrogen atom.[19] This implies that the BDE_{OH} of the [Fe^{IV}(O)(Por$^{+\bullet}$)]$^{+}$ system will be considerably smaller than that of P450 CpdI and unable to react via hydrogen atom abstraction. Indeed, we calculate a BDE_{OH} for the reaction of ^{3}[Fe^{III}(OH)(Por$^{+\bullet}$)]$^{+}$ into CpdI and a hydrogen atom of ΔE+ZPE = 66.3 kcal mol^{-1}, whereas for a P450 CpdI model a value of 88.9 kcal mol^{-1} was obtained.[20] In aliphatic hydroxylation the energy of the hydrogen atom abstraction step is equal to the difference in BDE_{CH} of the substrate and the BDE_{OH} of the oxidant. The BDE_{CH} of ethylbenzene is 82.5 kcal mol^{-1}.[14b] In the case of [Fe^{IV}(O)(Por$^{+\bullet}$)]$^{+}$, therefore, hydrogen atom abstraction from ethylbenzene will be endothermic by 16.2 kcal mol^{-1}, whereas the P450 CpdI model should give an exothermic hydrogen atom abstraction by –6.4 kcal mol^{-1}. Indeed, the radical intermediate ^{4}**I**$_H$ for ethylbenzene as a substrate is 14.4 kcal mol^{-1} higher in energy than reactants and, therefore, matches the difference in energy between BDE_{OH} and BDE_{CH} of oxidant and substrate. The endothermicity for the hydrogen atom abstraction reactions of substrates by [Fe^{IV}(O)(Por$^{+\bullet}$)]$^{+}$ is too high and, therefore; this process will not be able to compete with lower energy reaction channels, such as substrate epoxidation and aromatic hydroxylation.

Thus, the efficiency and reaction rate constant of aliphatic hydroxylation was shown to be linearly correlated with BDE_{OH},[19b] hence, the system without axial ligand, i.e. [Fe^{IV}(O)(Por$^{+\bullet}$)]$^{+}$, has reduced catalytic efficiency for aliphatic hydroxylation. Clearly, the axial cysteinate ligand in P450 enzymes affects the reactivity properties of the oxo group and, thereby makes it a better oxidant. Electrophilic reactions, such as aromatic hydroxylation and epoxidation, however, tend to connect with the ionization energy of the substrate and the electron affinity of the oxidant,[21] which is appropriate for [Fe^{IV}(O)(Por$^{+\bullet}$)]$^{+}$ to perform these reactions.

Discussion

In this work a comprehensive overview of arene activation by [Fe^{IV}(O)(Por$^{+\bullet}$)]$^{+}$ and [Fe^{IV}(O)(TPFPP$^{+\bullet}$)]$^{+}$ is given as mimics of P450 CpdI reactivity with substrates. As some of the substrates have aliphatic substituents to the arene, our initial work focused on establishing the nature of the reaction products. Unfortunately, aliphatic and aromatic hydroxylation of arenes gives products with equal mass and as such cannot be distinguished by mass spectrometry. Moreover, the fragmentation patterns of the products did not give direct evidence of what pathway was followed either. Hence, FT-ICR MS cannot distinguish the two products directly. We, therefore, repeated the experiments with deuterium labelled compounds, which gave only minor changes to the rate constants and implicated that the rate determining step does not include a hydrogen atom abstraction.

To gain further insight into the details of the reaction mechanism and the bifurcation processes computational modelling was performed. In particular, DFT studies on the relative barriers for aliphatic versus aromatic hydroxylation reactions were performed (Figures 4 and 5) and confirmed the latter to be well lower in energy. As such, in the gas-phase the [Fe^{IV}(O)(TPFPP$^{+\bullet}$)]$^{+}$ complex will preferentially react via aromatic hydroxylation over aliphatic hydroxylation with substrates. Nam et al[22] studied the aliphatic versus aromatic hydroxylation of ethylbenzene by [Fe^{IV}(O)(TPFPP$^{+\bullet}$)(X)] with X = Cl^{-}/$CF_3SO_3^{-}$ in dichloromethane. Aliphatic hydroxylation products were obtained with [Fe^{IV}(O)(TPFPP$^{+\bullet}$)(Cl)] as an oxidant, whereas aromatic hydroxylation products were detected in a reaction with [Fe^{IV}(O)(TPFPP$^{+\bullet}$)(CF_3SO_3)]. Subsequent computational modelling showed that the axial ligand affects the electron affinity and O–H bond strength (bond dissociation energy, BDE_{OH}) and hence affected the relative barriers of aliphatic

versus aromatic hydroxylation.[14b,23] To gain further insight into the intricate details of the bifurcation processes, below we will show a molecular orbital and valence bond interpretation of the mechanisms, but first we will discuss the experimental reaction trends.

To find trends and a rationale in the obtained rate constants and particularly find evidence on the properties of the catalyst/oxidant that determines the reaction process, we decided to search for physicochemical properties of substrate and oxidant in correlation with the rate constant. These analyses should give insight into the fundamental properties of P450 CpdI and how it is able to activate arenes. To this end, we decided to plot the natural logarithm of the rate constant against physical chemical properties of the substrate and oxidant, including the ionization energy of the substrate. Thus, previously it was shown that reactions starting with a rate-determining hydrogen atom abstraction generally correlate with the strength of the C–H bond that is broken, i.e. the bond dissociation energy (BDE_{CH}).[24,25] However, aromatic hydroxylation pathways by metal-oxo complexes were shown to connect to the ionization energy (IE) of the substrate.[25]

Figure 6 displays plots of the natural logarithm of the experimentally determined rate constant versus the ionization energy of the substrate (part a) and the BDE_{CH} value of the aliphatic group of the substrate (part b). As can be seen from Figure 6, the ionization energy of the substrate follows a linear correlation with the ln k_{exp} value with an R^2 value of 0.88. Interestingly, the rate constants for benzene and naphthalene activation by $[Fe^{IV}(O)(TPFPP^{+\bullet})]^+$ do not fit the trend. This may be due to the fact that these substrates approach the oxidant differently and give extra interactions with the oxidant. Aromatic hydroxylation, similarly to double bond epoxidation, therefore, gives rate constants that are proportional to the IE of the substrate involved.[25] This means that any oxidant reacting with a substrate containing an arene and a double bond as a separate group will give preferential aromatic hydroxylation rather than double bond epoxidation.

For the set of substrates with aliphatic substituents also a plot of ln k_{exp} versus BDE_{CH} was attempted (Figure 6b), however, no correlation is found. Based on this evidence the aliphatic hydroxylation pathway can be ruled out as a viable mechanism for arene activation by $[Fe^{IV}(O)(TPFPP^{+\bullet})]^+$ and based on the reactivity trends as well as the KIE values, the dominant pathway is aromatic hydroxylation.

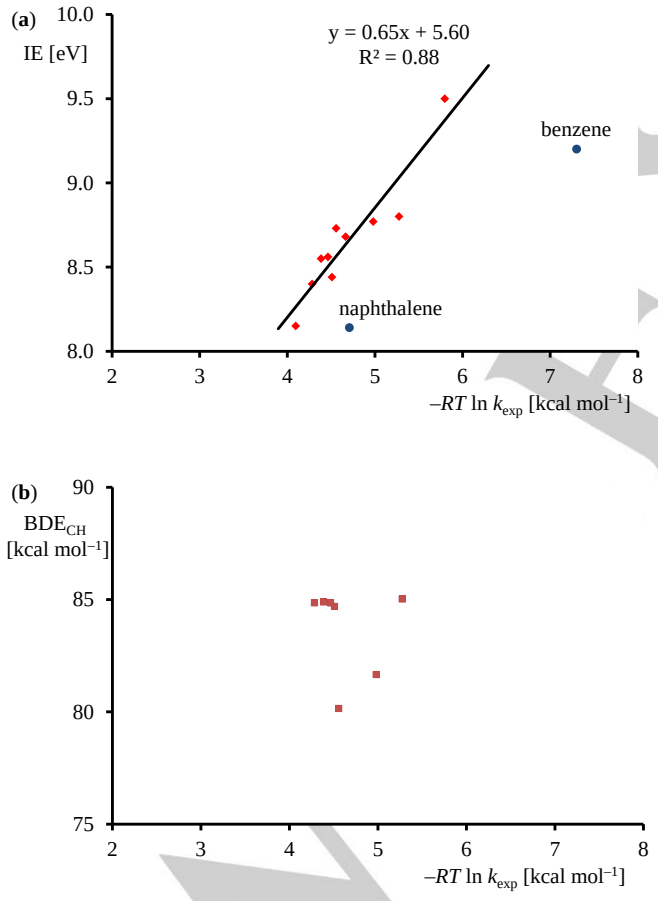

Figure 6. Correlation of the natural logarithm of the rate constant with (a) ionization energy from the substrate. (b) BDE_{CH} value of the aliphatic group of the substrate. Ionization energies taken from the NIST Database.[13] BDE_{CH} values calculated with DFT at B3LYP/BS2//UB3LYP/BS1 including ZPE corrections.

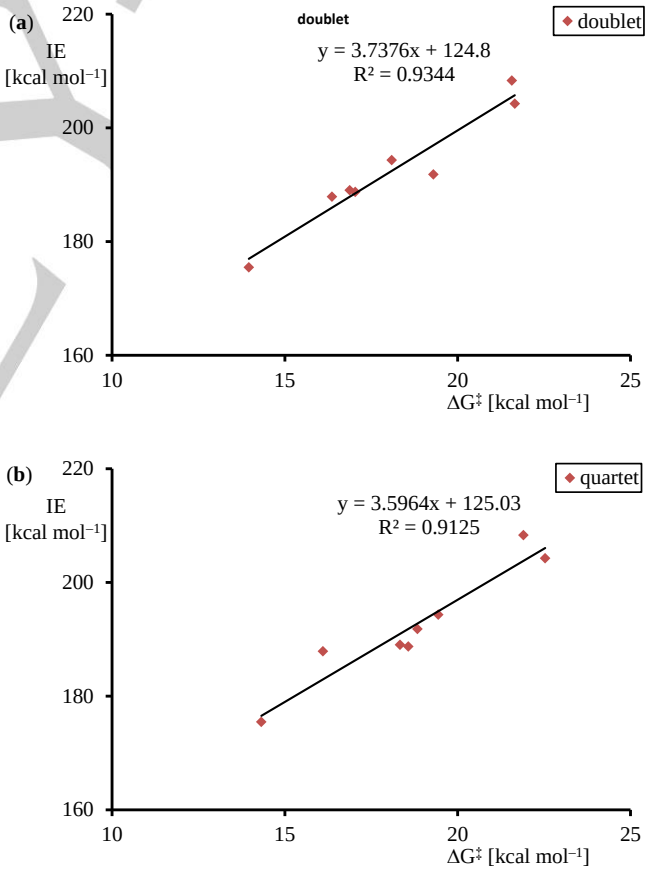

Figure 7. Correlation of the computationally determined free energy of activation of aromatic hydroxylation (**TS1**) with calculated ionization energy of the substrate.

Figure 7 gives the corresponding plot for the correlation between the ionization energy and the computationally determined aromatic hydroxylation free energy of activation calculated for the various ^{4,2}**TS1** structures for the substrates in Figure 4. In agreement with the experimental result, a linear correlation between barrier height and ionization energy is found with an R^2 = 0.91 (quartet) and 0.93 (doublet). As such, both experimental reaction rates and computational barrier heights implicate a linear correlation between the natural logarithm of the rate constant and ionization energy. As both experiment and theory give the same correlation, of course, the experimental rates also correlate linearly with the computational barrier heights. Moreover, using the found trends, this enables us to predict reaction rates of alternative substrates. For instance, the rate constants for aromatic hydroxylation of chlorobenzene and fluorobenzene could not be measured. However, the trend from Figures 6a and 7a enable us to predict their values as 4.8 and 5.0 × 10^{-11} (cm^3 $molecule^{-1}$ s^{-1}) respectively. Similarly, we predict barrier heights at B3LYP level of theory from the experimental trend in Figure 6a of ΔG = 19.5, 19.9 and 24.4 kcal mol^{-1} for i-propylbenzene, t-butylbenzene and benzaldehyde, respectively, whereas values of ΔG = 18.8, 19.2 and 19.3 kcal mol^{-1} are expected for m-, o-, and p-xylene. As such the two plots from Figure 6 and 7 enable one to predict experimental rates from computational trends or computational barriers from experimental trends. To verify the accuracy of this procedure we predicted the DFT barriers for toluene, ethylbenzene and mesitylene from the trend in Figure 6a and find values of ΔG = 22.3, 21.2 and 16.4 kcal mol^{-1}, respectively, which are within a mean error of 2.8 kcal mol^{-1} of the DFT calculated results (Supporting Information).

Electronically, the fact that the trends correlate with ionization energy implicate that the electron transfer from substrate to oxidant will determine the reaction rate. The trends in reactivity also imply that none of the products observed in the mass spectra can correlate with aliphatic hydroxylation products. Therefore, the product ions with m/z 1028 and m/z 1150 (Figure 2) originate from the aromatic hydroxylation of substrates. Clearly, product release from the iron(III) complex is a slow process and a mixture of metal ligated and free phenol products are obtained.

Evidently, the rate constant and reactivity patterns of the iron(IV)-oxo porphyrin complex with arenes is dependent on key properties of the oxidant and substrate. In order to improve catalyst design and find novel oxidants for this reaction process, we delineated the transition state barrier into fundamental properties of oxidant and substrate. This analysis identifies the origin of the reaction mechanism and explains how the oxidant can be further improved for better catalysis.

To understand the obtained trends and correlations we used a parabolic approximation of previously described VB models to explain the reaction barrier.[26] Figure 8 displays the basic features of the two-parabola crossing model, where we assume the reactant complex (**R**) to reside in a local minimum that can be described by a parabola with function $y_R = ax^2$ with y_R being the energy function of the reactant complex, x the reaction coordinate and a is a constant that describes the curvature of the reaction coordinate function. The reactant complex is defined as the starting point of the reaction with coordinates x_R = 0 and y_R = 0. For the product complex we describe the potential energy surface with another parabola that is shifted from the reactant parabola and hence has function $y_P = bx^2 + cx + d$ with b, c, and d some constants that describe the curvature and extremes of the parabola. We now assume that the product local minimum is located at a reaction coordinate with value x = 1 and the transition state at the half-way point (x = ½). That means the two curves for y_R and y_P will cross at x_{cross} = ½ and create a crossing point, at energy y_P(½) = ΔE_{cross}, which will ultimately lead to an avoided crossing and a transition state for the reaction. One can see from Figure 8 that $y_P(0) = d = E_{FC,\mathbf{R}}$, whereby $E_{FC,\mathbf{R}}$ represents the Franck-Condon energy at the reactant geometry. Furthermore, $y_P(1)$ is equal to the driving force for the reaction (ΔE_{rp}). Using the information for the first derivative of y_P at the point x = 1, i.e. $y_P'(1) = 0$, we can now derive Eq 4 for y_P(½) as a function of the driving force for the reaction and the Franck-Condon energy at the reactants geometry.

$$y_P(½) = \Delta E_{cross} = \frac{1}{4}E_{FC,\mathbf{R}} + \frac{3}{4}\Delta E_{rp} \qquad (4)$$

The actual transition state, however, with energy $\Delta E^{‡}$ will be below the crossing point by an amount B that represents the resonance energy, Eq 5.

$$\Delta E^{‡} = \Delta E_{cross} - B \qquad (5)$$

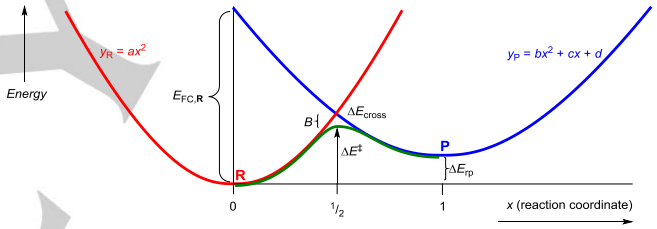

Figure 8. Two-parabola curve crossing model for the prediction of barrier heights.

Using Eqs 4 and 5 we can predict the barrier height for the reaction in terms of the driving force for the reaction (ΔE_{rp}), the change in electronic configuration between the reactant and product state in the geometry of the reactants ($E_{FC,\mathbf{R}}$) and the resonance energy B. Values for the driving force are taken as the difference in energy (ΔE+*ZPE*) between reactant complex (**R**) of ^{4}CpdI and substrate with the radical intermediate ^{4}**I1**.

Figure 9 shows the curve crossing diagram with key valence bond (VB) structures of critical points along the reaction mechanism. The difference in VB structure between the reactant and product structures in the geometry of the reactants will determine the value of $E_{FC,\mathbf{R}}$. These diagrams have been used previously to rationalize barrier heights of chemical reactions and explain what features of substrate and oxidant affect the value of the barrier height.[21,27]

The diagram starts on the bottom-left with the reactant configuration of $[Fe^{IV}(O)(Por^{+\bullet})]^+$ and arene. Thus, in the ground state the system has three unpaired electrons distributed over the π^*_{xz}, π^*_{yz} and a_{1u} molecular orbitals. The π_{xz}/π^*_{xz} and π_{yz}/π^*_{yz} molecular orbitals represent the bonding and antibonding combinations of 3d orbitals on Fe with 2p orbitals on oxygen.

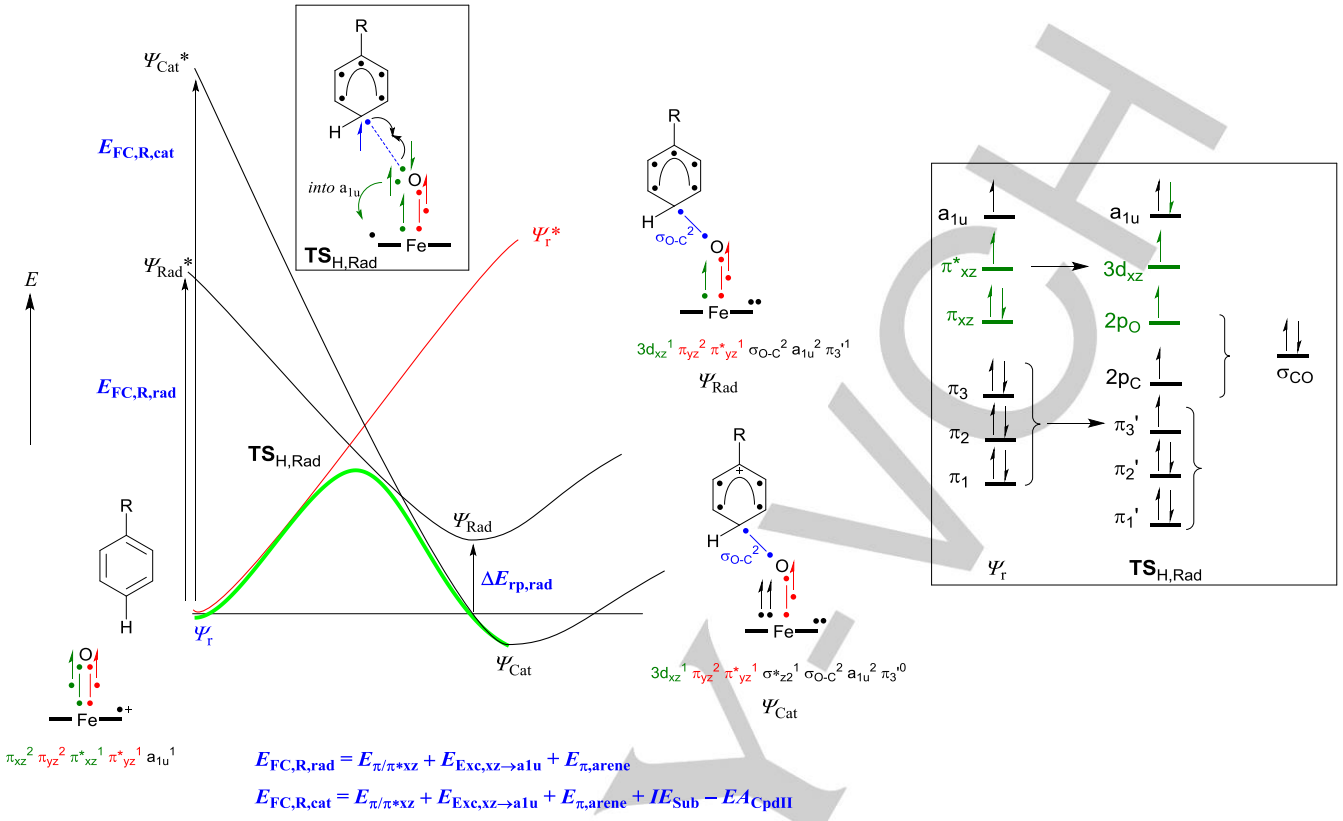

Figure 9. Valence bond curve crossing diagram and orbital/bonding changes along the electrophilic addition pathway of arene activation by $[Fe^{IV}(O)(Por^{+\bullet})]^{+}$. Valence bond structures give electrons as dots. Orbital occupation and hybridization changes are indicated with the orbital diagram.

The a_{1u} orbital is a nonbonding π-orbital on the porphyrin ring and is close in energy to the a_{2u} orbital. In previous work on $[Fe^{IV}(O)(Por^{+\bullet})]^{+}$ we found several close-lying electronic states with either doublet or quartet spin and single occupation of a_{1u} or a_{2u}.[12] The three green dots along the Fe–O bond in Figure 9 represent the π_{xz}/π^*_{xz} electrons, while the ones in red are the π_{yz}/π^*_{yz} electrons. Both set of π/π* orbitals form a three-electron bond along the Fe–O group. Upon formation of the intermediate complex either a radical or cationic structure is formed. In both cases the C–O bond is formed from one of the electrons of the π-cloud of the substrate plus an electron from the π_{xz}/π^*_{xz} system. This means that electrophilic addition will result in the breaking of the π-system of the substrate and the set of six electrons in the substrate π-system (π_1, π_2 and π_3 orbitals), will be split into a $2p_C$ atomic orbital for one carbon and a conjugated π-system over the remaining five carbon atoms with orbitals π_1', π_2' and π_3'. Breaking the π-cloud of the substrate, will cost the system an energy $E_{\pi,arene}$. Of course, the breaking of the π-cloud will also be correlated to the excitation energy in the π-system as well as the ionization energy for removal of an electron from one of the π-orbitals.

As such, the barrier height and the driving force for the reaction are likely to correlate with the ionization energy of the substrate as indeed shown in Figure 6a and 7. By contrast, the cationic pathway will more likely be connected to the second ionization energy of the substrate as apart from the breaking of the π-orbitals of the substrate also an electron will have to transfer to the oxidant.

In the calculations presented in Figures 3 and 4 the intermediates are of a cationic nature with an electronic configuration of $3d_{xz}^1\ \pi_{yz}^2\ \pi^*_{yz}^1\ \sigma^*_{z2}^1\ a_{1u}^2\ \pi'^0_3$ with spin density of less than 0.1 on the aromatic ring and a value of about 3 on the FeO unit. Interestingly, the transition states gives significant radical character on the aromatic ring, typically 0.50 – 0.70, so that these transition states should be considered as radical-type transition states connecting the reactants with the radical intermediates. For the estimation of the barrier heights from the VB structures, therefore, we will use the driving force to reach the radical intermediates, $\Delta E_{rp,rad}$. On the oxidant side of the reaction, a number of electron transfer and orbital reorganizations happen, which enable us to predict the value for $E_{FC,R,rad}$. Firstly, the π_{xz}/π^*_{xz} set of orbitals (highlighted in green in the VB structures for the reactant and the transition state) split back into atomic orbitals ($3d_{xz}$ and $2p_O$), which will cost the system E_{π/π^*xz} in energy. One of the electrons of $2p_O$ pairs up with the single electron in $2p_C$ and forms the new C–O bonding orbital σ_{CO}. The value of E_{π/π^*xz} is determined from the relative energies of the two orbitals in the reactant complex and is 85.2 kcal mol^{-1}. The remaining two electrons stay on the metal-porphyrin side of the system and one of those electrons is promoted into the a_{1u} orbital to fill it with a second electron with excitation energy $E_{Exc,xz\rightarrow a1u}$. From the relative energies of the π_{xz} and a_{1u} orbitals in the reactant complex a value of 51.5 kcal mol^{-}

^{1} is obtained. Finally, the Franck-Condon energy between the reactant and the radical state is dependent on the breaking of the π-system of the arene, $E_{\pi,arene}$. The overall Franck-Condon energy for the transition from the reactant to the radical state is given in Eq 6.

$$E_{FC,\mathbf{R},rad} = E_{\pi/\pi^*xz} + E_{Exc,xz\rightarrow a1u} + E_{\pi,arene} \quad (6)$$

Using Eqs 4 – 6 we have estimated VB predicted barrier heights of ΔE+ZPE = 12.5, 12.1, 5.1 and 6.2 kcal mol^{-1} for the reaction of $[Fe^{IV}(O)(Por^{+\bullet})]^+$ with chlorobenzene, fluorobenzene, toluene and ethylbenzene, respectively. These values are in good quantitative agreement with those obtained from full DFT optimizations and shown in Figures 3 and 4 above. As such, the two-parabola curve crossing diagram gives a good quantitative representation of the reaction mechanism and the kinetics obtained. Moreover, the model gives hints on the key electronic properties of oxidant and substrate that determine the rate determining reaction step.

Eq 6 shows that the barrier height for aromatic hydroxylation should be proportional to the excitation energy of the π-cloud of the substrate arene, which, of course, is proportional to the ionization energy. Indeed that is what we observe above in Figures 6 and 7. The fact that the rate constants for benzene and naphthalene do not fit the trend displayed in Figure 6 could be explained as those systems following a cationic pathway rather than a more radical pathway and hence should correlate with $E_{FC,\mathbf{R},cat}$ rather than $E_{FC,\mathbf{R},rad}$.

In the case of electrophilic addition, however, there is also a pathway leading to a cationic intermediate with wave function Ψ_{Cat}. This electronic configuration can be formed from the radical intermediate through an electron transfer from the substrate π-system into the σ^*_{z2} orbital of the metal. As such, we expect there to be a direct transition state leading to the radical intermediate as well as one to form the cationic intermediate, although the latter is higher in energy. These transition states will be proportional to the Franck-Condon energy from the reactant state to the excited state representing the product electronic configuration. Figure 8 gives descriptions for the Franck-Condon energies reaching the radical state ($E_{FC,\mathbf{R},rad}$) and the one leading to the cationic state ($E_{FC,\mathbf{R},cat}$). Based on the electronic differences between ground and excited state configurations, we established the individual contributions determining these excitation energies. As it happens, the excitation energy leading to the cationic state contains all features of the one leading to the radical state plus two additional terms, namely the ionization energy of the substrate (IE_{Sub}) and the electron affinity of the metal in the radical intermediate, which is the reduced form of the iron(IV)-oxo species, namely EA_{CpdII}. Therefore, in the transition state the cationic process is higher in energy and only after the barrier a crossover from radical to cationic pathway will be observed leading to the cationic intermediate and fast conversion to phenol products. The DFT and VB models, therefore, implicate a rate determining electrophilic addition step with a radical-type transition state. However, upon C–O bond formation en route to the intermediate a state crossing occurs to the lower lying cationic intermediate.

In summary, the VB diagram highlights the factors of the substrate and oxidant that affect the barrier height and predicts that the rate constant is proportional to the ionization energy of the substrate regarded that the oxidant stays the same.

Conclusions

A combined FT-ICR MS and DFT study is performed on the reactivity of arenes with a model of P450 CpdI without axial ligand. It is shown that removal of the axial ligand gives a dominant aromatic hydroxylation pathway and no evidence of aliphatic hydroxylation is found. In general, the natural logarithm of the rate constant of aromatic hydroxylation links linearly with the ionization energy of the substrate. The explanation of this finding is supported within the framework of a Valence Bond model.

Experimental Section

Materials. All chemicals and solvents used for this work were research grade and purchased from commercial sources. Iodosylbenzene was used as a terminal oxidant for the synthesis of the iron(IV)-oxo complex and was generated according to a literature procedure,[29] and subsequently stored at –20°C prior to usage.

Instrumental. A Bruker BioApex FT-ICR mass spectrometer was used for all experiments described here, which includes a cylindrical infinity cell, a 4.7 T superconducting magnet and an Apollo I electrospray ionization (ESI) source. Analyte solutions of reactants were infused into the mass spectrometer through a fused-silica capillary with internal diameter of 50 μm at a continuous flow rate of 120 μL h^{-1} by a syringe pump. Ions were desolvated by applying an N_2 counter current drying gas heated at 380K and then accumulated for 0.8 seconds in a radiofrequency-only hexapole ion guide. Thereafter, the ions were pulsed into the ICR cell that is held at room temperature (300 K). The ions of interest, $[Fe^{IV}(O)(TPFPP^{+\bullet})]^+$ at m/z 1044, were mass selected by ion ejection procedures and ion-molecule reactions were studied by inserting neutral collision gases and monitoring the abundance of product ions as a function of time. Neutral reagents were admitted into the FT-ICR cell at stationary pressures (in the range from 1.0 – 15 × 10^{-8} mbar) by a needle valve. The pressure in the FT-ICR cell was measured with a cold-cathode sensor (IKR Pfeiffer Balzers S.p.A., Milan, Italy) and calibrated against the rate constant of proton transfer from methane cation radical to methane, Eq 7, which is known to have a rate constant k = 1.1 × 10^{-9} cm^3 s^{-1}.[29]

$$CH_4^{+\bullet} + CH_4 \rightarrow CH_5^+ + CH_3^\bullet \quad (7)$$

In the mass spectra, corrections for ^{13}C isotopic contributions were applied in order to reveal possible species deriving from a hydrogen atom transfer channel, namely $[Fe^{IV}(OH)(TPFPP)]^+$ ions at m/z 1045, presenting a formally protonated ferryl unit.

Ion abundances were monitored as a function of time and pseudo first-order rate constants were obtained from the slope of the semi-logarithmic plots. These values, determined at least in triplicate, were then converted into second-order rate constants (k_{exp}) by dividing the parent ion abundances by the substrate concentration at 300 K. Reaction efficiencies (Φ) were calculated from the ratio of the second-order rate constant and the collision rate constant (k_{ADO}), Eq 8. Values for k_{ADO} were calculated using the parametrized trajectory theory.[30]

$$\Phi = k_{exp}/k_{ADO} \times 100\% \quad (8)$$

Product ion branching ratios and reaction efficiencies were found to be independent of the pressure in the ICR cell. The error in the estimated second-order rate constants (k_{exp}) is to within 10% with an absolute error of ±30%, caused largely by the uncertainty affecting the pressure of the neutral.[31]

Sample preparation. The $[Fe^{IV}(O)(TPFPP^{+\bullet})]^+$ ion was synthesized in a methanol/dichloromethane (1:1) mixture by adding iodosylbenzene (0.5 mM) to the corresponding iron(III)chloride complex, 10 μM of $[Fe^{III}(TPFPP)Cl]$, and cooled to –40°C. The iron(IV)-oxo complex remained stable at this temperature for at least 1 hour. The ESI FT-ICR mass analysis of the reaction mixture gave a prominent peak centered at m/z 1044 with isotopic pattern conforming to an iron(IV)-oxo complex, $[Fe^{IV}(O)(TPFPP^{+\bullet})]^+$, together with the reduced form $[Fe^{III}(TPFPP)]^+$ at m/z 1028. Nonetheless, the ion population at m/z 1044 comprises a fraction of isomeric species, likely corresponding to an isobaric ion oxidized on the porphyrin ring, and unable to attain any oxidation process. This fraction was titrated by its complete trapping by NO yielding the $[Fe^{III}(TPFPP–O)(NO)]^+$ adduct, in analogy with the reduced form, $[Fe^{III}(TPFPP)]^+$. The presence of this unreactive form was taken into account in treating the kinetic data.

Computation. To support the experimental observations and determine further trends and features of the reaction mechanism, we did a detailed DFT study on aromatic hydroxylation by $[Fe^{IV}(O)(Por^{+\bullet})]^+$, where Por represents an unsubstituted porphyrin ligand. We also tested the full $[Fe^{IV}(O)(TPFPP^{+\bullet})]^+$ system but found very little differences in geometry, electronic description and reactivity with respect to the $[Fe^{IV}(O)(Por^{+\bullet})]^+$ system (Supporting Information Figure S4), hence the latter was used here. All calculations were performed in Gaussian-09,[32] and implemented DFT methods. Test calculations with a range of density functional methods show little sensitivity of the amount of exchange and correlation to optimized geometries and the potential energy landscape gives the same pattern (Supporting Information Tables S1 – S20), therefore, we will show results obtained with the B3LYP[33] density functional method only as that will enable a direct comparison with our previous work.[12]

Initial geometry optimizations and constraint geometry scans were performed at the UB3LYP/BS1 level of theory: BS1 is LACVP on iron (with core potential) and 6-31G on the rest of the atoms.[34] The maxima of the geometry scans were then used as starting points for the transition state searches, which established first-order saddle points with a single imaginary frequency for the correct mode. Improved energies were obtained through single point calculations at the UB3LYP/BS2 level of theory: BS2 is LACV3P+ on iron (with core potential) and 6-311+G* on the rest of the atoms. Free energies are reported at a temperature of 298K and 1atm pressure and include zero-point, thermal and entropic corrections under standard conditions. Although the experiments were performed in the gas-phase, we also tested the effect of solvent on the obtained rate constants from single point calculations using the polarized continuum model in Gaussian with a dielectric constant mimicking acetonitrile. All structures represent full geometry optimizations without constraints and were characterized with a frequency calculation as either a local minimum (real frequencies only) or a first-order saddle point.

Acknowledgements

MAS and FGCR thank the Petroleum Technology Development Fund and the Conacyt Mexico for a studentship. SdV acknowledges cpu time support from the National Service of Computational Chemistry Software (NSCCS). The EU-COST Network Explicit Control Over Spin-states in Technology and Biochemistry (ECOSTBio, CM1305) is acknowledged for support. MEC and SF are grateful to the Università di Roma „La Sapienza“ for funding of the FT-ICR MS work.

Keywords: Fourier transform-ion cyclotron resonance • Mass spectrometry • Density functional theory • Arene • Oxygen atom transfer

[1] a) M. Costas, M. P. Mehn, M. P. Jensen, L. Que Jr, *Chem. Rev*. **2004**, *104*, 939-986; b) M. M. Abu-Omar, A. Loaiza, N. Hontzeas, *Chem. Rev*. **2005**, *105*, 2227-2252; c) W. Nam, *Acc. Chem. Res*. **2007**, *40*, 522–531; d) P. Comba, M. Kerscher, *Coord. Chem. Rev*. **2009**, *253*, 564–574; e) I*ron-containing enzymes: Versatile catalysts of hydroxylation reaction in nature* (Eds.: S. P. de Visser, D. Kumar), RSC Publishing, Cambridge (UK), **2011**.

[2] a) E. I. Solomon, T. C. Brunold, M. I. Davis, J. N. Kemsley, S. K. Lee, N. Lehnert, F. Neese, A. J. Skulan, Y. S. Yang, J. Zhou, *Chem. Rev*. **2000**, *100*, 235-349; b) S. V. Kryatov, E. V. Rybak-Akimova, S. Schindler, *Chem. Rev*. **2005**, *105*, 2175–2226; c) P. C. A. Bruijnincx, G. van Koten, R. J. M. Klein Gebbink, *Chem. Soc. Rev*. **2008**, *37*, 2716–2744; d) M. Costas, *Coord. Chem. Rev*. **2011**, *255*, 2912–2932; e) A. R. McDonald, L. Que Jr, *Coord. Chem. Rev*. **2013**, *257*, 414–428; f) W. Nam, Y.-M. Lee, S. Fukuzumi, *Acc. Chem. Res*. **2014**, *47*, 1146–1154.

[3] A. Karlsson, J. V. Parales, R. E. Parales, D. T. Gibson, H. Eklund, S. Ramaswamy, *Science* **2003**, *299*, 1039–1042.

[4] a) T. D. H. Bugg, *Tetrahedron* **2003**, *59*, 7075–7101; b) E. G. Kovaleva, J. D. Lipscomb, *Science* **2007**, *316*, 453–457; c) S. Fetzner, R. A. Steiner, *Appl. Microbiol. Biotechnol*. **2010**, *86*, 791–804.

[5] a) M. Sono, M. P. Roach, E. D. Coulter, J. H. Dawson, *Chem. Rev*. **1996**, *96*, 2841–2888; b) J. T. Groves, *Proc. Natl. Acad. Sci. USA* **2003**, *100*, 3569–3574; c) B. Meunier, S. P. de Visser, S. Shaik, *Chem. Rev*. **2004**, *104*, 3947–3980; d) *Cytochrome P450: Structure, Mechanism and Biochemistry* (Ed.: P. R. Ortiz de Montellano) 3rd Ed., Kluwer Academic/Plenum Publishers, New York, **2005**; e) A. W. Munro, H. M. Girvan, K. J. McLean, *Nat. Prod. Rep*. **2007**, *24*, 585–609; f) G. Grogan, *Curr. Opin. Chem. Biol*. **2011**, *15*, 241–248; g) *Handbook of Porphyrin Science* (Eds.: K. M. Kadish, K. M. Smith, R. Guilard), World Scientific Publishing Co., New Jersey, **2010**; h) T. L. Poulos, *Chem. Rev*. **2014**, *114*, 3919–3962.

[6] a) S. Shaik, D. Kumar, S. P. de Visser, A. Altun, W. Thiel, *Chem. Rev*. **2005**, *105*, 2279–2328; b) M. R. A. Blomberg, T. Borowski, F. Himo, R.-Z. Liao, P. E. M. Siegbahn, *Chem. Rev*. **2014**, *114*, 3601–3658.

[7] a) F. Lanucara, M. E. Crestoni, *Chem. Eur. J*. **2011**, *17*, 12092–12100; b) M. E. Crestoni, S. Fornarini, F. Lanucara, J. J. Warren, J. M.; Mayer, *J. Am. Chem. Soc*. **2010**, *132*, 4336–4343; c) B. Chiavarino, R. Cipollini, M. E. Crestoni, S. Fornarini, F. Lanucara, A. Lapi, *J. Am. Chem. Soc*. **2008**, *130*, 3208–3217; d) M. E. Crestoni, S. Fornarini, F. Lanucara, *Chem. Eur. J*. **2009**, *15*, 7863–7866; e) M. E. Crestoni, S. Fornarini, *Inorg. Chem*. **2005**, *44*, 5379–5387.

[8] M. E. Crestoni, S. Fornarini, *Inorg. Chem*. **2007**, *46*, 9018–9020.

[9] J. Rittle, M. T. Green, *Science* **2010**, *330*, 933–937.

[10] a) M. T. Green, *J. Am. Chem. Soc*. **1999**, *121*, 7939–7940; b) F. Ogliaro, N. Harris, S. Cohen, M. Filatov, S. P. de Visser, S. Shaik, *J. Am. Chem. Soc*. **2000**, *122*, 8977–8989; c) D. Li, Y. Wang, K. Han, *Coord. Chem. Rev*. **2012**, *256*, 1137–1150; d) S. P. de Visser, *Adv. Inorg. Chem*. **2012**, *64*, 1–31.

[11] K. Kuhnel, N. Ke, M. J. Cryle, S. G. Sligar, M. A. Schuler, I. Schlichting, *Biochemistry* **2008**, *47*, 6552–6559.

[12] M. A. Sainna, S. Kumar, D. Kumar, S. Fornarini, M. E. Crestoni, S. P. de Visser, *Chem. Sci*. **2015**, *6*, 1516–1529.

[13] NIST Chemistry WebBook, *NIST Standard Reference Database*, Number 69 (Eds.: P. J. Linstrom, W. G. Mallard) National Institute of Standards and Technology, Gaithersburg MD, 20899, http://webbook.nist.gov .

[14] a) S. P. de Visser, S. Shaik, *J. Am. Chem. Soc*. **2003**, *125*, 7413–7424; b) S. P. de Visser, R. Latifi, L. Tahsini, W. Nam, *Chem. Asian J*. **2011**, *6*, 493–504.

[15] Asaka, M.; Fujii, H. *J. Am. Chem. Soc*. **2016**, *138*, 8048–8051.

[16] S. Kumar, A. S. Faponle, P. Barman, A. K. Vardhaman, C. V. Sastri, D. Kumar, S. P. de Visser, *J. Am. Chem. Soc*. **2014**, *136*, 17102–17115.
[17] L. Ji, A. S. Faponle, M. G. Quesne, M. A. Sainna, J. Zhang, A. Franke, D. Kumar, R. van Eldik, W. Liu, S. P. de Visser, *Chem. Eur. J*. **2015**, *21*, 9083–9092.
[18] Pratter, S. M.; Konstantinovics, C.; DiGiuro, C. L. M.; Leitner, E.; Kumar, D.; de Visser, S. P.; Grogan, G.; Straganz, G. D. Angew. Chem. Int. Ed. 2013, 52, 9677–9681.
[19] a) J. M. Mayer, *Acc. Chem. Res*. **1998**, *31*, 441–450; b) S. P. de Visser, *J. Am. Chem. Soc*. **2010**, *132*, 1087–1097.
[20] S. P. de Visser, L.-S. Tan, *J. Am. Chem. Soc*. **2008**, *130*, 12961–12974.
[21] D. Kumar, B. Karamzadeh, G. N. Sastry S. P. de Visser, *J. Am. Chem. Soc*. **2010**, *132*, 7656–7667.
[22] W. J. Song, Y. O. Ryu, R. Song, W. Nam, *J. Am. Chem. Soc*. **2005**, *10*, 294–304.
[23] S. P. de Visser, *Chem. Eur. J*. **2006**, *12*, 8168–8177.
[24] a) J. M. Mayer, *Annu. Rev. Phys. Chem*. **2004**, *55*, 363–390; b) J. Kaizer, E. J. Klinker, N. Y. Oh, J.-U. Rohde, W. J. Song, A. Stubna, J. Kim, E. Münck, W. Nam, L. Que Jr., *J. Am. Chem. Soc*. **2004**, *126*, 472–473; c) J. Yoon, S. A. Wilson, Y. K. Jang, M. S. Seo, K. Nehru, B. Hedman, K. O. Hodgson, E. Bill, E. I. Solomon, W. Nam, *Angew. Chem. Int. Ed*. **2009**, *48*, 1257–1260; d) D. P. Goldberg, *Acc. Chem. Res*. **2007**, *40*, 626–634; e) Y. Kang, H. Chen, Y. J. Jeong, W. Lai, E. H. Bae, S. Shaik, W. Nam, *Chem. Eur. J*. **2009**, *15*, 10039–10046.
[25] a) S. Shaik, P. Milko, P. Schyman, D. Usharani, H. Chen, *J. Chem. Theory Comput*. **2011**, *7*, 327–339; b) D. Kumar, G. N. Sastry, S. P. de Visser, *J. Phys. Chem. B* **2012**, *116*, 718–730.
[26] a) S. S. Shaik, *J. Am. Chem. Soc*. **1981**, *103*, 3692–3701; b) S. Shaik, *Phys. Chem. Chem. Phys*. **2010**, *12*, 8706–8720.
[27] a) S. Shaik, D. Kumar, S. P. de Visser, *J. Am. Chem. Soc*. **2008**, *130*, 10128–10140; b) D. Kumar, R. Latifi, S. Kumar, E. V. Rybak-Akimova, M. A. Sainna, S. P. de Visser, *Inorg. Chem*. **2013**, *52*, 7968–7979.
[28] H. Saltzman, J. G. Sharefkin, *Organic Syntheses*, Wiley, New York, **1973**, Collect. Vol. 5, p 658.
[29] a) M. Meot-Ner, in *Gas Phase Ion Chemistry*, (Ed.: M. T. Bowers), Academic Press, New York, **1979**; Vol. 1; b) J. E. Bartmess, R. M. Georgiadis, *Vacuum* **1983**, *33*, 149–154.
[30] T. Su, W. J. Chesnavich, *J. Chem. Phys*. **1982**, *76*, 5183–5185.
[31] F. Angelelli, B. Chiavarino, M. E. Crestoni, *J. Am. Soc. Mass Spectrom*. **2005**, *16*, 589–598.
[32] M. J. Frisch, *Gaussian* 09, revision D.01; Gaussian, Inc., Wallingford, CT, 2004.
[33] a) A. D. Becke, *J. Chem. Phys*. **1993**, *98*, 5648–5652; b) C. Lee, W. Yang, R. G. Parr, *Phys. Rev. B* **1988**, *37*, 785–789.
[34] a) P. J. Hay, W. R. Wadt, *J. Chem. Phys*. **1985**, *82*, 270–283; b) W. J. Hehre, R. Ditchfield, J. A. Pople, *J. Chem. Phys*. **1972**, *56*, 2257–2261.

Entry for the Table of Contents

Layout 1:

FULL PAPER

A combined mass spectrometry and density functional theory study on aromatic hydroxylation by a cytochrome P450 Compound I model is presented. Details of the mechanism are elucidated from kinetics, isotope effect and computational studies and show that the rate constant correlates with the ionization energy of the oxidant.

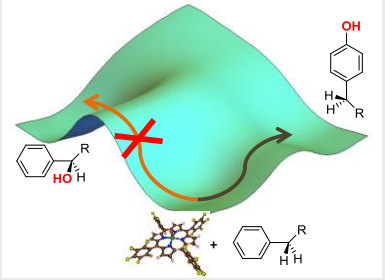

Fabián G. Cantú Reinhard, Mala A. Sainna, Pranav Upadhayay, Devesh Kumar, Simonetta Fornarini, Maria Elisa Crestoni,* and Sam P. de Visser**

Page No. – Page No.

A systematic account on aromatic hydroxylation by a cytochrome P450 model Compound I: A low-pressure mass spectrometry and computational study